ChemComm

ROYAL SOCIETY OF CHEMISTRY

COMMUNICATION

View Article Online
View Journal | View Issue

Check for updates

Cite this: *Chem. Commun.*, 2024, **60**, 1004

Received 28th November 2023,
Accepted 21st December 2023

DOI: 10.1039/d3cc05781j

rsc.li/chemcomm

Enhanced photocatalytic hydrogen evolution through MoS_2 quantum dots modification of bismuth-based perovskites†

Yunjian Fan,[a] Jingmiao Hu,[bc] Tianyang Li,[d] Shuang Xu,[d] Shan Chen *[a] and Huajie Yin *[b]

Efficient and cost-effective photocatalysts are pivotal for advancing large-scale solar hydrogen generation. Herein, we report a composite photocatalyst by incorporating MoS_2 quantum dots (MoS_2 QDs) as a cocatalyst into $Cs_3Bi_2I_9$, resulting in a high enhancement in photocatalytic performance. Remarkably, the optimum MoS_2 QDs/$Cs_3Bi_2I_9$ composite achieves an impressive hydrogen evolution rate (6.09 mmol h^{-1} g^{-1}) in an ethanol and HI/H_3PO_2 mixed solution. This rate is 8.8 times higher than pristine $Cs_3Bi_2I_9$ (0.69 mmol h^{-1} g^{-1}) and notably surpasses Pt/$Cs_3Bi_2I_9$ (2.47 mmol h^{-1} g^{-1}). Moreover, the composite displays exceptional stability during an 18-hour reaction, showcasing its potential for sustainable photocatalytic hydrogen evolution.

The urgent need for sustainable energy due to extensive fossil fuel use has sparked interest in harnessing solar energy as a renewable solution.[1] Photocatalytic hydrogen evolution, a promising pathway for generating clean hydrogen from sunlight, faces challenges like efficiency, stability, and cost, underscoring the crucial importance of developing high-performance and cost-effective photocatalysts to drive innovation in this technology.[2–5] Lead halide perovskites (LHPs) have gained significant attention as efficient photocatalysts in the past five years, exhibiting favorable visible light absorption, exceptionally-long charge-carrier diffusion length when employed for photocatalytic fuel production and chemical synthesis.[6–11] However, the presence of toxic lead (Pb) in LHPs severely limits their potential for practical application. Therefore, researchers are exploring alternatives like Sn and Bi metals to replace Pb within halide perovskite structures. Despite this, the introduction of Sn^{2+} often leads to instability, while Bi^{3+} shows promise due to its similar isoelectric state to Pb^{2+} and success in stabilizing bismuth-based halide perovskites.[12–16] However, the severe charge recombination due to the high exciton binding energy of Bi-based perovskite photocatalysts, results in their poor photocatalytic activity. For example, Zhao *et al.* reported the $MA_3Bi_2I_9$ photocatalyst for photocatalytic hydrogen evolution reaction (HER) in the saturated HI solution, which initially exhibited low hydrogen generation activity (12.19 μmol h^{-1} g^{-1}) and was subsequently improved (169.21 μmol h^{-1} g^{-1}) with Pt as a cocatalyst.[17] Nonetheless, its activity remains notably lower than that reported for LHP photocatalysts (1–20 mmol h^{-1} g^{-1}).

Recently, several non-noble metal co-catalysts, including rGO,[12] CoP,[18] BP,[9] Ni_3C,[10] and MoS_2 nanosheet,[19] have been introduced to the LHP photocatalysts and the resulting composite demonstrated an impressive photocatalytic performance improvement. It is widely acknowledged that their beneficial impact stems from the creation of various heterojunctions between lead perovskites and the co-catalyst, which effectively enhances the electron–hole separation efficiency and augments photocatalyst carrier transport rates.[20–22] Notably, although MoS_2 quantum dots (QDs) have proven to be a high-performance, sustainable, and cost-effective alternative to Pt for electrocatalytic and photocatalytic HER applications,[23–25] their potential as a cocatalyst to enhance the photocatalytic HER activity of Bi-based perovskite photocatalysts remains unexplored.

Herein, we present a composite of $Cs_3Bi_2I_9$ perovskite microcrystals modified with MoS_2 QDs for efficient photocatalytic hydrogen generation *via* HI splitting in an HI/ethanol solution. The photocatalytic performance of the MoS_2 QDs/$Cs_3Bi_2I_9$ composite demonstrated an impressive rate of 6.09 mmol h^{-1} g^{-1} for hydrogen evolution, surpassing pristine $Cs_3Bi_2I_9$ (0.69 mmol h^{-1} g^{-1}) by 8.8 times and Pt/$Cs_3Bi_2I_9$ (2.47 mmol h^{-1} g^{-1}) by 2.5 times. Notably,

---

[a] Institutes of Physical Science and Information Technology, Anhui University, Hefei, 230039, China. E-mail: chenshan@ahu.edu.cn
[b] Key Laboratory of Materials Physics, Centre for Environmental and Energy nanomaterials, Anhui Key Laboratory of Nanomaterials and Nanotechnology, CAS Center for Excellence in Nanoscience, Institute of Solid State Physics, Hefei Institutes of Physical Science, Chinese Academy of Sciences, Hefei 230031, China, Hefei, 230031, China. E-mail: yinhj@issp.ac.cn
[c] University of Science and Technology of China, Hefei, Anhui, 230026, People's Republic of China
[d] School of Materials Science and Engineering, Anhui University, Hefei, 230039, China

† Electronic supplementary information (ESI) available. See DOI: https://doi.org/10.1039/d3cc05781j

this activity level represents a new record among Bi-based perovskite photocatalysts under visible-light conditions. This heightened activity is attributed to the superior HER active sites provided by MoS_2 QDs as co- catalysts, combined with the unique crystal structure of $Cs_3Bi_2I_9$, ensuring the creation of MoS_2 QDs/$Cs_3Bi_2I_9$ heterojunctions of a type II nature.

We employed a modified solvothermal approach to synthesize high-quality $Cs_3Bi_2I_9$ microcrystals (method details in the supporting information).[26] Additionally, MoS_2 QDs were synthesized *via* a solvothermal treatment of bulk MoS_2 in isopropanol, followed by a sequence of centrifugal separation.[27] The MoS_2 QDs/$Cs_3Bi_2I_9$ heterostructure composites were obtained by ultrasonic mixing $Cs_3Bi_2I_9$ microcrystals into the isopropanol dispersion of MoS_2 QDs followed by solvent evaporation. The zeta potential of $Cs_3Bi_2I_9$ microcrystals and MoS_2 QDs is 10.57 and −9.39 mV, respectively (Fig. S1, ESI†). Thus, the negatively charged MoS_2 QDs were electrostatic self-assembly onto the surface of the positively charged $Cs_3Bi_2I_9$ after ultrasonication and solvent evaporation, as illustrated in Fig. 1a. The resulting composite contained MoS_2 QDs with a mass percentage of 5.4 wt%. Pristine $Cs_3Bi_2I_9$, as illustrated in Fig. S2 (ESI†), exhibited a regular hexagonal prism shape with sizes ranging from 500 nm to 1 μm. The XRD pattern (Fig. S3, ESI†) confirms its excellent crystallinity, with peak positions matching the standard perovskite structure of $Cs_3Bi_2I_9$ (JCPDS#23-0847). TEM images of MoS_2 QDs revealed their size to be between 2 nm and 5 nm (Fig. S4, ESI†), and XPS spectra illustrated the presence of both the 1T phase and 2H phase (Fig. S5, ESI†).[28] After incorporating MoS_2 QDs, the resulting MoS_2 QDs/$Cs_3Bi_2I_9$ composites maintained their hexagonal prism shape (Fig. 1b) and crystallinity. TEM and HRTEM images revealed tight attachment of MoS_2 QDs (yellow circles) to the surface of $Cs_3Bi_2I_9$ crystals (Fig. 1c and Fig. S6, ESI†).

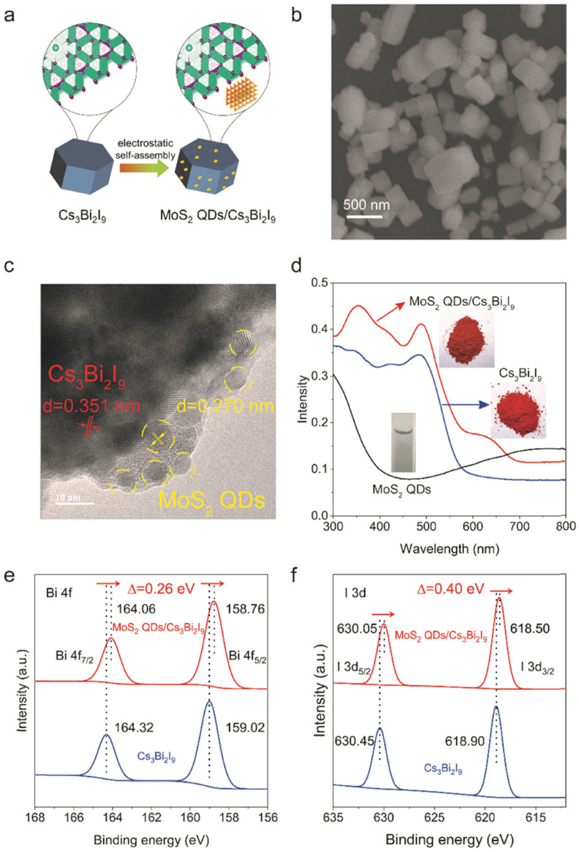

Fig. 1 (a) Schematic illustration of synthetic route for the MoS_2 QDs/$Cs_3Bi_2I_9$. (b) SEM images of MoS_2 QDs/$Cs_3Bi_2I_9$. (c) TEM image of the MoS_2 QDs/$Cs_3Bi_2I_9$. (d) UV-vis diffuse reflectance spectra of $Cs_3Bi_2I_9$, MoS_2 QDs, and MoS_2 QDs/$Cs_3Bi_2I_9$ (inset: product pictures) (e) and (f) XPS spectra of Bi 4f and I 3d region of $Cs_3Bi_2I_9$ and MoS_2 QDs/$Cs_3Bi_2I_9$.

In the inset image of Fig. 1d, $Cs_3Bi_2I_9$ exhibited a vibrant red color, while the color of MoS_2 QDs/$Cs_3Bi_2I_9$ was slightly deepened. Their UV-vis diffuse reflectance spectra (UV-vis-DRS) further indicated extended light absorption in the range of 600–800 nm due to the presence of MoS_2 QDs. In comparison to pristine $Cs_3Bi_2I_9$, the measured band gap of MoS_2 QDs/$Cs_3Bi_2I_9$ was reduced to 1.81 eV from the Kubelka–Munk plot (Fig. S7, ESI†). The presence of MoS_2 QDs in the $Cs_3Bi_2I_9$/MoS_2 QDs composite was further confirmed by XPS survey spectra, including the Bi 4f and I 3d regions (Fig. 1e, f and Fig. S8, ESI†). The high-resolution Bi 4f and I 3d peaks of MoS_2 QDs/$Cs_3Bi_2I_9$ shifted towards lower binding energies (0.26 eV for Bi 4f and 0.40 eV for I 3d), respectively, compared to pristine $Cs_3Bi_2I_9$. These shifts could be attributed to the strong interfacial interaction between MoS_2 QDs and $Cs_3Bi_2I_9$, as reported in previous studies.[20–22,29]

The photocatalytic hydrogen evolution performance of MoS_2 QDs/$Cs_3Bi_2I_9$ (5 mg) and the comparison samples was measured in a 20 mL ethanol solution containing 0.2 mL of HI and 0.2 mL of H_3PO_2 under visible light irradiation ($\lambda > 420$ nm, 300-W Xe lamp). H_3PO_2 is used as a sacrificial reagent in the reaction system to reduce I_3^- ions to form I-. The generated H_2 increased linearly with irradiation time, reaching a peak hydrogen evolution rate of 6.09 mmol h^{-1} g^{-1} over a 3-hour reaction period. The apparent quantum efficiency (AQE) of MoS_2 QDs/$Cs_3Bi_2I_9$ for H_2 evolution at 500 nm was determined to be 4.71%.[30] When the MoS_2 QDs/$Cs_3Bi_2I_9$ composite was replaced with an equal amount of pristine $Cs_3Bi_2I_9$ while maintaining other experimental conditions, the average achieved H_2 evolution rate dramatically dropped to 0.69 mmol h^{-1} g^{-1}. This observation indicates that the enhanced photocatalytic activity of MoS_2 QDs/$Cs_3Bi_2I_9$ originates from the incorporation of MoS_2 QDs. Furthermore, Pt-loaded $Cs_3Bi_2I_9$ (Pt/$Cs_3Bi_2I_9$) and bulk MoS_2-modified $Cs_3Bi_2I_9$ exhibited H_2 evolution rates of 2.47 (Fig. S9, ESI†) and 1.93 mmol h^{-1} g^{-1}, respectively, which were notably lower than that of MoS_2 QDs/$Cs_3Bi_2I_9$, highlighting the superior cocatalytic performance of MoS_2 QDs over Pt and bulk MoS_2. Consequently, the photocatalytic HER activity of MoS_2 QDs/$Cs_3Bi_2I_9$ is over 8.8 and 2.4 times higher than that of $Cs_3Bi_2I_9$ and Pt/$Cs_3Bi_2I_9$, respectively. As illustrated in Fig. 2c, the effect of different mass percentages of MoS_2 QDs in the MoS_2 QDs/$Cs_3Bi_2I_9$ composite was investigated. Notably, the incorporation of just 0.9 wt% MoS_2 QDs into $Cs_3Bi_2I_9$ led to a significant increase in the H_2 evolution rate to 3.67 mmol h^{-1} g^{-1}. With higher MoS_2 QDs loading, the H_2 evolution rate progressively increased, peaking at 6.09 mmol h^{-1} g^{-1} for the MoS_2 QDs/$Cs_3Bi_2I_9$ composite with

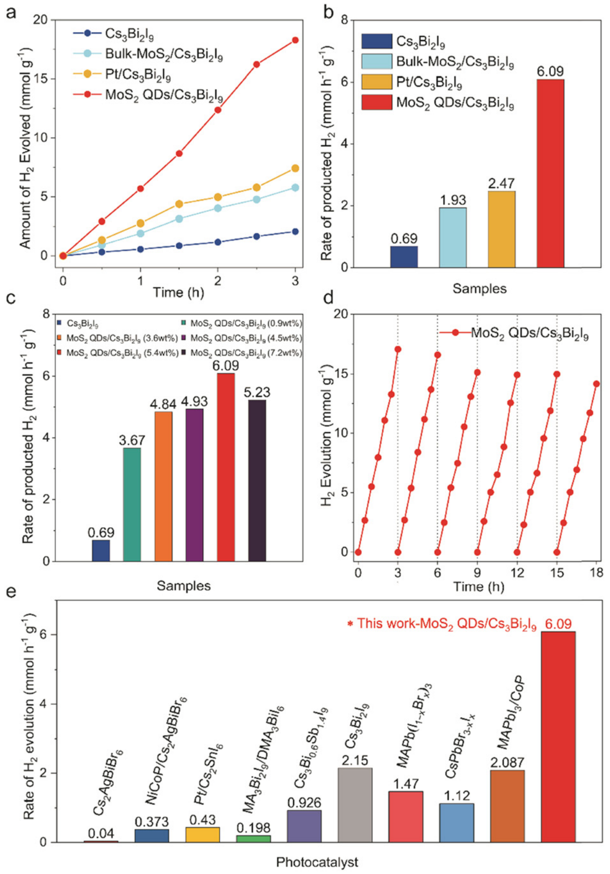

Fig. 2 (a) Time courses of photocatalytic H_2 evolution over $Cs_3Bi_2I_9$, bulk-MoS_2/$Cs_3Bi_2I_9$, Pt/$Cs_3Bi_2I_9$, MoS_2 QDs/$Cs_3Bi_2I_9$ ($\lambda > 420$ nm). (b) The H_2 generation rate of $Cs_3Bi_2I_9$, bulk-MoS_2/$Cs_3Bi_2I_9$, Pt/$Cs_3Bi_2I_9$, MoS_2 QDs/$Cs_3Bi_2I_9$. (c) The H_2 generation rate of MoS_2 QDs/$Cs_3Bi_2I_9$ loading different amounts of cocatalyst (0.9, 3.6, 4.5, 5.4, 7.2 wt%). (d) Cycling measurements of photocatalytic H_2 production of MoS_2 QDs/$Cs_3Bi_2I_9$ ($\lambda > 420$ nm). (e) Comparison of the hydrogen evolution performance of reported perovskite-based catalysts and this work.

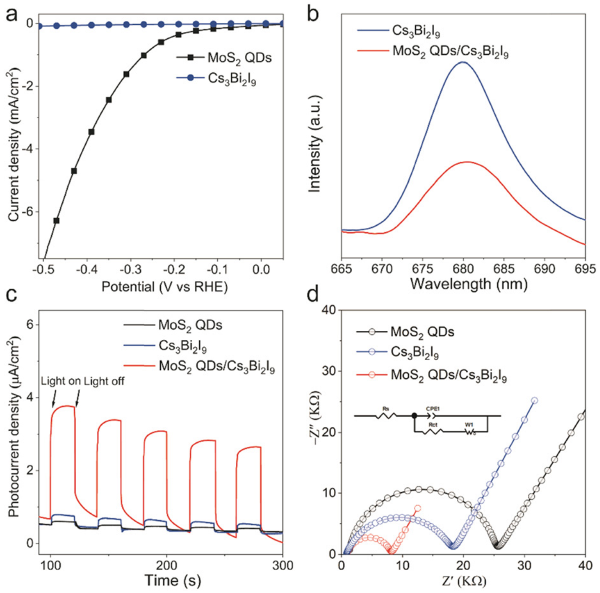

Fig. 3 (a) Electrochemical HER polarization curves of $Cs_3Bi_2I_9$ and MoS_2 QDs loaded carbon paper recorded in HI solution. (b) PL spectra of $Cs_3Bi_2I_9$ and MoS_2 QDs/$Cs_3Bi_2I_9$. (c) Transient photocurrent responses of $Cs_3Bi_2I_9$, MoS_2 QDs and MoS_2 QDs/$Cs_3Bi_2I_9$ recorded in 0.1 M tetrabutylammonium hexafluorophosphate ethanol solution under light irradiation. (d) EIS Nyquist plots of $Cs_3Bi_2I_9$ and MoS_2 QDs/$Cs_3Bi_2I_9$ under light irradiation.

5.4 wt% MoS_2 QDs. However, at 7.2 wt% MoS_2 QDs, the photocatalytic HER activity showed a decline.

In addition to its impressive photocatalytic hydrogen evolution activity, the MoS_2 QDs/$Cs_3Bi_2I_9$ composite also exhibited remarkable stability (Fig. 2d). Throughout six cycles of 3-hour experiments, the rate of photocatalytic hydrogen evolution remained nearly constant. XRD patterns displayed no alterations in the crystalline phase of the MoS_2 QDs/$Cs_3Bi_2I_9$ composite after an 18-hour reaction, and SEM analysis confirmed the preservation of its morphology (Fig. S10, ESI†). Furthermore, the MoS_2 QDs/$Cs_3Bi_2I_9$ composite outperformed recently reported Bi-based perovskite photocatalysts and some of Pb-based perovskite photocatalysts in terms of photocatalytic hydrogen evolution (Fig. 2e and Table. S1, ESI†).[7,13,23–25,29,31,32]

Both electrochemical and photoelectrochemical experiments were employed to elucidate the significant effect of MoS_2 QDs in enhancing the photocatalytic hydrogen evolution activity of $Cs_3Bi_2I_9$. From Fig. 3a, it can be found that the electrocatalytic HER onset potential of MoS_2 QDs could reach ~ -0.2 V *vs.* RHE indicating a superior HER activity of MoS_2 QDs compared with pristine $Cs_3Bi_2I_9$. Moreover, the photoluminescence (PL) emission intensity of MoS_2 QDs/$Cs_3Bi_2I_9$ exhibited a notable reduction compared to that of pristine $Cs_3Bi_2I_9$ (Fig. 3b). Time-resolved photoluminescence (TRPL) results show that the average lifetime for MoS_2 QDs/$Cs_3Bi_2I_9$ is greater than $Cs_3Bi_2I_9$ (Fig. S11, ESI†). This suggests that the association with MoS_2 QDs significantly enhances the separation efficiency of electrons and holes within $Cs_3Bi_2I_9$, thereby substantially boosting the photocatalytic HER efficacy of MoS_2 QDs/$Cs_3Bi_2I_9$. Notably, the MoS_2 QDs/$Cs_3Bi_2I_9$ composite demonstrated the highest photocurrent, directly correlating with its most favorable catalytic H_2 evolution activity (Fig. 3c). Furthermore, for a deeper understanding of the improved HER activity of the photocatalyst, we employed electrochemical impedance spectroscopy (EIS) to characterize and analyze the opto-electronic performance of the photocatalysts in terms of the separation and transfer of photogenerated charges. EIS analysis revealed that the MoS_2 QDs/$Cs_3Bi_2I_9$ composite displayed significantly lower charge transfer resistance compared to pristine $Cs_3Bi_2I_9$ (Fig. 3d).

Based on the ultraviolet photoelectron spectroscopy (UPS), we obtained E_{VB} and E_{CB} values of 1.1 V (NHE), -0.92 V (NHE) and 3.54 V (NHE), -0.11 V (NHE) for $Cs_3Bi_2I_9$ and MoS_2 QDs, respectively (Fig. S12 and S13, ESI†). The energy diagram of the MoS_2 QDs/$Cs_3Bi_2I_9$-based hydrogen generation system through HI splitting is illustrated in Fig. 4.[10,18,19,33] According to the UPS calculation method, we obtained the Fermi levels (E_f) values of 0.12 V for $Cs_3Bi_2I_9$ and 0.52 V for MoS_2 QDs. A type II heterojunction forms at the interface of MoS_2 QDs and

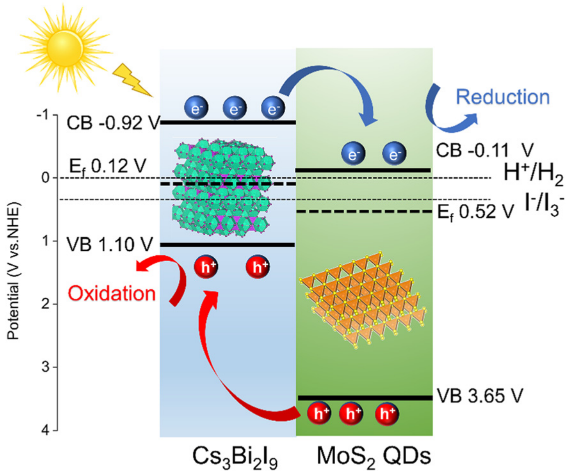

Fig. 4 Schematic band diagram of $Cs_3Bi_2I_9$ and MoS_2 QDs for photocatalytic HI splitting reactions.

$Cs_3Bi_2I_9$, leading to efficient migration of photogenerated electrons to MoS_2 QDs, thus facilitating the effective separation of photogenerated carriers. Simultaneously, these photogenerated electrons on the surface of MoS_2 QDs diffuse toward active sites where protons undergo efficient reduction to generate H_2. These heterojunctions play a pivotal role in promoting the separation of charge carriers, thereby contributing significantly to the remarkable enhancement in activity.

In summary, the incorporation of MoS_2 QDs as cocatalysts has been demonstrated to significantly enhance the photocatalytic performance of $Cs_3Bi_2I_9$ for hydrogen evolution. The optimized MoS_2 QDs/$Cs_3Bi_2I_9$ composite showcases an impressive 8.8-fold increase in the rate of H_2 evolution compared to the unmodified $Cs_3Bi_2I_9$. This study underscores the potential of harnessing zero-dimensional MoS_2 QDs as remarkably efficient cocatalysts, to enhance the efficacy of the photocatalytic HER in Bi-based perovskite photocatalysts. Furthermore, the insights gleaned from this research pave the way for the development of exceptionally active photocatalysts based on lead-free perovskites.

This work was financially supported by the National Natural Science Foundation of China (52102197, 52102325), Excellent Research and Innovation Team Project of Anhui Province (2023AH010001) and Collaborative Innovation Program of Hefei Science Center, CAS (2022HSC-CIP016).

Conflicts of interest

There are no conflicts to declare.

Notes and references

1 K. Sivula and R. Krol, *Nat. Rev. Mater.*, 2016, **1**, 15010.
2 Q. Wang and K. Domen, *Chem. Rev.*, 2020, **120**, 919–985.
3 M.-Y. Qi, M. Conte, M. Anpo, Z.-R. Tang and Y.-J. Xu, *Chem. Rev.*, 2021, **121**, 13051–13085.
4 S. Chen, H. Yin, P. Liu, Y. Wang and H. Zhao, *Adv. Mater.*, 2023, **35**, 2203836.
5 M. Liu, M. B. Johnston and H. J. Snaith, *Nature*, 2013, **501**, 395–398.
6 S. Park, W. J. Chang, C. W. Lee, S. Park, H.-Y. Ahn and K. T. Nam, *Nat. Energy*, 2016, **2**, 16185.
7 Z. Guan, Y. Wu, P. Wang, Q. Zhang, Z. Wang, Z. Zheng, Y. Liu, Y. Dai, M.-H. Whangbo and B. Huang, *Appl. Catal., B*, 2019, **245**, 522–527.
8 S. Bera, S. Ghosh, T. Maiyalagan and R. N. Basu, *ACS Appl. Energy Mater.*, 2022, **5**, 3821–3833.
9 X. Deng, X. Kuang, J. Zeng, B. Zi, Y. Ma, R. Yan, J. Zhang, B. Xiao and Q. Liu, *Nanotechnology*, 2022, **33**, 175401.
10 Z. Zhao, J. Wu, Y.-Z. Zheng, N. Li, X. Li and X. Tao, *ACS Catal.*, 2019, **9**, 8144–8152.
11 Y. Wu, P. Wang, X. Zhu, Q. Zhang, Z. Wang, Y. Liu, G. Zou, Y. Dai, M.-H. Whangbo and B. Huang, *Adv. Mater.*, 2018, **30**, 1704342.
12 T. Wang, D. Yue, X. Li and Y. Zhao, *Appl. Catal., B*, 2020, **268**, 118399.
13 P. Zhou, H. Chen, Y. Chao, Q. Zhang, W. Zhang, F. Lv, L. Gu, Q. Zhao, N. Wang, J. Wang and S. Guo, *Nat. Commun.*, 2021, **12**, 4412.
14 D. Wu, B. Huo, Y. Huang, X. Zhao, J. Yang, K. Hu, X. Mao, P. He, Q. Huang and X. Tang, *Small*, 2022, **18**, e2106001.
15 B.-M. Bresolin, P. Sgarbossa, D. W. Bahnemann and M. Sillanpää, *Sep. Purif. Technol.*, 2020, **251**, 117320.
16 Z. Zhang, Y. Yang, Y. Wang, L. Yang, Q. Li, L. Chen and D. Xu, *Angew. Chem., Int. Ed.*, 2020, **132**, 18293–18296.
17 Y. Guo, G. Liu, Z. Li, Y. Lou, J. Chen and Y. Zhao, *ACS Sustainable Chem. Eng.*, 2019, **7**, 15080–15085.
18 C. Cai, Y. Teng, J.-H. Wu, J.-Y. Li, H.-Y. Chen, J.-H. Chen and D.-B. Kuang, *Adv. Funct. Mater.*, 2020, **30**, 2001478.
19 X. Zhao, S. Chen, H. Yin, S. Jiang, K. Zhao, J. Kang, P. F. Liu, L. Jiang, Z. Zhu, D. Cui, P. Liu, X. Han, H. G. Yang and H. Zhao, *Matter*, 2020, **3**, 935–949.
20 Y. Jiang, J.-F. Liao, H.-Y. Chen, H.-H. Zhang, J.-Y. Li, X.-D. Wang and D.-B. Kuang, *Chemistry*, 2020, **6**, 766–780.
21 J. Ran, H. Zhang, S. Fu, M. Jaroniec, J. Shan, B. Xia, Y. Qu, J. Qu, S. Chen, L. Song, J. M. Cairney, L. Jing and S. Z. Qiao, *Nat. Commun.*, 2022, **13**, 4600.
22 B. Xia, B. He, J. Zhang, L. Li, Y. Zhang, J. Yu, J. Ran and S. Z. Qiao, *Adv. Energy Mater.*, 2022, **12**, 2201449.
23 Y. Ji, M. She, X. Bai, E. Liu, W. Xue, Z. Zhang, K. Wan, P. Liu, S. Zhang and J. Li, *Adv. Funct. Mater.*, 2022, **32**, 2201721.
24 Y. Tang, C. H. Mak, R. Liu, Z. Wang, L. Ji, H. Song, C. Tan, F. Barrière and H.-Y. Hsu, *Adv. Funct. Mater.*, 2020, **30**, 2006919.
25 Z. Zhao, J. Wu, Y.-Z. Zheng, N. Li, X. Li, Z. Ye, S. Lu, X. Tao and C. Chen, *Appl. Catal., B*, 2019, **253**, 41–48.
26 M. Li, S. Xu, L. Wu, H. Tang, B. Zhou, J. Xu, Q. Yang, T. Zhou, Y. Qiu, G. Chen, G. I. N. Waterhouse and K. Yan, *ACS Energy Lett.*, 2022, **7**, 3370–3377.
27 L. Najafi, B. Taheri, B. Martín-García, S. Bellani, D. Di Girolamo, A. Agresti, R. Oropesa-Nuñez, S. Pescetelli, L. Vesce, E. Calabrò, M. Prato, A. E. Del Rio Castillo, A. Di Carlo and F. Bonaccorso, *ACS Nano*, 2018, **12**, 10736–10754.
28 Z. Zhao, J. Wu, Y.-Z. Zheng, N. Li, X. Li, Z. Ye, S. Lu, X. Tao and C. Chen, *Appl. Catal., B*, 2019, **253**, 41–48.
29 G. Chen, P. Wang, Y. Wu, Q. Zhang, Q. Wu, Z. Wang, Z. Zheng, Y. Liu, Y. Dai and B. Huang, *Adv. Mater.*, 2020, **32**, e2001344.
30 J. Yang, A. Acharjya, M.-Y. Ye, J. Rabeah, S. Li, Z. Kochovski, S. Youk, J. Roeser, J. Grüneberg, C. Penschke, M. Schwarze, T. Wang, Y. Lu, R. van de Krol, M. Oschatz, R. Schomäcker, P. Saalfrank and A. Thomas, *Angew. Chem., Int. Ed.*, 2021, **60**, 19797–19803.
31 Q. Huang, Y. M. Guo, J. X. Chen, Y. B. Lou and Y. X. Zhao, *New J. Chem.*, 2022, **46**, 7395–7402.
32 Y. Zhang, Z. Sun, Z. Wang, Y. Zang and X. Tao, *Int. J. Hydrogen Energy*, 2022, **47**, 8829–8840.
33 S. A. Shah, I. Khan and A. Yuan, *Molecules*, 2022, **27**, 3289.